Research article

Highly stable CsPbBr₃/ PMA perovskite nanocrystals for improved optical performance

Purusottam Reddy Bommireddy [a], Jagadeesh Babu B [b], Sreedhar Sunku [b], Kamal Basha C [c], Youngsuk Suh [a], Chandra Sekhar M [b,**], Si-Hyun Park [a,*]

[a] *Department of Electronic Engineering, Yeungnam University, 280 Daehak-ro, Gyeongsan-si, Gyeongsanbuk-do, South Korea*
[b] *Department of Physics, Madanapalle Institute of Technology and Science, Madanapalle, 517325, India*
[c] *Department of Electrical and Electronics Engineering, Madanapalle Institute of Technology and Science, Madanapalle, 517325, India*

ABSTRACT

In this study, to address the stability issues, we synthesized a CsPbBr₃-coated poly (maleic anhydride-alt-1-octadecene) (CsPbBr₃/PMA) using a modified hot-injection method. The CsPbBr₃/PMA perovskite nanocrystals (PNCs) exhibited effective green emission at 522 nm with an improved photoluminescence quantum yield (86.8 %) compared to traditional CsPbBr₃ PNCs (54.2 %). The ligands in the polymer coating can bond with the uncoordinated Pb and Br ions on the surface of PNCs to minimize surface defects and avoid exposure to the external environment, enhancing the stability of the perovskites. Time-resolved photoluminescence spectra showed longer lifetimes for CsPbBr₃/PMA PNCs, while transient absorption measurements provided valuable insights into the intraband hot-exciton relaxation and recombination. We demonstrate the potential application of CSPbBr₃/PMA in a down-conversion white-light-emitting diode (LED) by coupling green CsPbBr₃/PMA and red $K_2SiF_6:Mn^{4+}$ phosphor-coated glass slides onto a 455-nm blue GaN LED. The white LED produced a white light with the International Commission on Illumination color coordinates of (0.323, 0.345), luminous efficiency of 58.4 lm/W, and color rendering index of 83.2. The fabricated, white-LED system obtained a wide color gamut of 125.3 % of the National Television Standards Committee and 98.9 % of Rec. 2020. The findings demonstrate that CsPbBr₃/PMA can be an efficient down-conversion material for white LEDs and backlighting.

1. Introduction

Metal halide perovskite nanocrystals (PNCs) have evolved as a fascinating class of materials in optoelectronics because of their unique and excellent optical and electrical properties, which include a narrow-band and tunable emission, high photoluminescence quantum yield (PLQY), direct band gap, defect tolerance, high absorption coefficients, long carrier lifetimes, and high charge carrier mobilities make them as active components for lasers, solar cells, light-emitting diodes (LEDs) and X-ray scintillators [1–5]. However, despite their significant optical characteristics, CsPbBr₃ PNCs still suffer from inherent stability issues upon exposure to environmental conditions that lead to degradation of the nanocrystals, reduced efficiency, diminished optical properties, and limited device lifetime.

---

* Corresponding author.
** Corresponding author.
E-mail addresses: chandu.phys@gmail.com (C.S. M), sihyun_park@ynu.ac.kr (S.-H. Park).

Researchers have been actively investigating methods to improve the stability of CsPbBr$_3$ PNCs by doping, growth of oxide shells, incorporating them into a composite structure with suitable matrix materials, capping with inorganic stable matrices such as silica, alumina and polymers [6–11]. Using CsPbBr$_3$ nanocrystals for color conversion, rather than electroluminescent (EL) LEDs, is regarded as a more practical and less resource-intensive approach for developing nanocrystal LEDs, considering both material stability and ease of processing. This method reduces charging and thermal stress issues as no current flows through the layer, commonly seen in EL LEDs. The standard process involves blending PNCs with a thermo-curable silicone resin and integrating it into the LED. The existence of hydrophobic-organic ligands and solvents can impede the polymerization of the encapsulating resin; as a result, the mechanical stability of the material decreases. For lead halide perovskites, this is particularly troublesome as they need an abundance of organic ligands to avoid aggregation, reducing their QY and light emission [12–14]. To address these stability issues, polymer encapsulation is considered a better strategy to suppress surface defects and is employed for LED color conversion layers.

Among the various strategies being explored, encapsulating CsPbBr$_3$ nanocrystals within polymer matrices, such as poly (maleic anhydride-alt-1-octadecene) (PMA), poly (methyl methacrylate) (PMMA), polystyrene (PS), polycarbonate, acrylonitrile, butadiene, polyvinyl chloride, and styrene have gained much interest in the scientific community because the PNCs-polymer composite film offers an attractive solution for color-conversion optical films in the context of blue, green, red LEDs within the liquid-crystal display (LCD) backlight applications [15–18]. Moreover, the polymer layer acts as a barrier and effectively blocks the diffusion of moisture and oxygen into the nanocrystal structure, minimizing their detrimental effects on the electrical and optical properties of PNCs and preserving the structure [19,20]. Recent reports on various polymer matrices embedded with PNCs demonstrated promising results in addressing stability issues and improving the PL and lifetime of the CsPbBr$_3$ PNCs for white LED applications. Wang et al. synthesized (CsPbX$_3$, X = Br/I and I) PNCs incorporated PMMA films for stable and high-speed white light communication with a μLED chip [21]. Tong et al. employed a hot-injection method to synthesize lead halide PNCs incorporated into acrylic monomers, producing nanocrystal-polymer composite films characterized by remarkable stability and brightness [22]. Zhang et al. incorporated CsPbBr$_3$ PNCs into PS polymer nanofiber employing a one-step electrospinning process and demonstrated its effectiveness in enabling the high-efficiency detection of fluorescence in rhodamine solutions [23]. Babu et al. synthesized highly stable CsPbBr$_3$ incorporated poly (vinylidene fluoride)-co-hexafluoropropylene fibers employing electrospinning technique and studied the charge-transfer dynamics employing transient absorption (TA) spectroscopy. These results provided a number of photophysical insights and would pave the way for the development of flexible and highly efficient solar cells and photodetector devices [24]. Peng et al. synthesized polymer-encapsulated Zn-doped CsPbBr$_x$Cl$_{3-x}$ PNCs-based color converters to mitigate the challenges of blue overshoot and cyan gaps in white light-emitting diodes [25]. Adhikari et al. demonstrated that encapsulating metal halide perovskites in UV resin has enhanced their air, moisture, and light irradiation resistance and also achieved a color rendering index of 85 and luminous efficacy of ~349 lm/W [26]. Zhu et al. utilized a 3D printing technique to fabricate water-stable resin-perovskite-based RGB color conversion layers. The white LED fabricated using those RGB color conversion layers exhibited a color rendering index of 94 and a luminous efficacy of ~299 lm/W [27]. Ling et al. reported that poly (ethylene oxide) CsPbBr$_3$ PNCS using a spin-coating approach produced a remarkable PLQY of 60 %; moreover, it exhibited an electroluminescent efficiency above 53,000 cdm^{-2} [28].

PMA (poly (maleic anhydride-alt-1-octadecene) has proven to be an excellent ligand for encapsulating inorganic nanoparticles, such as magnetic, semiconductor, and gold nanoparticles that are coated initially with oleic acid or oleylamine. This ligand integrates within the carbon chain shell surrounding the nanoparticles, enhancing their stability. In cases where the nanoparticles have a stable core, the PMA units can undergo further polymerization with a diamine, allowing for the encapsulation of the nanoparticle core and its transfer to polar solvents [8,29]. In recent investigations, it has been found that the use of coating on CsPbBr$_3$ PNCs coated PMA (poly (maleic anhydride-alt-1-octadecene) exhibited improved stability and PL performance because of the effective passivation of surface defects in the PNCs. Meyns et al. synthesized PMA-coated cesium lead halide (CsPbX$_3$, X = Cl, Br, I) NCs. They discussed how PMA encapsulation passivated the NC surface and demonstrated their potential application in color conversion LEDs [8]. Li et al. synthesized stable β-CsPbI$_3$ incorporated PMA and achieved a remarkable PLQY of 89 %, and the corresponding red-emitting LED achieved a high external quantum efficiency of 17.8 % [30]. Xu et al. reported transient optical properties of CsPbX$_3$@PMA (X = Br, Br/I) perovskite quantum dots and achieved white light emission by integrating CsPbBr$_3$@PMA and CsPb(Br/I)$_3$@PMA films onto the blue LED chip [31]. Wu et al. documented that CsPbBr$_3$@PMA PNCs exhibited excellent stability against UV radiation, water, and exposure to air. They successfully developed a white LED device by combining CsPbBr$_3$@PMA PNCs with organic red luminescent phosphors on blue LED chips, delivering an impressive power efficiency of 56.6 lm/W [32].

In this study, we synthesized CsPbBr$_3$/PMA PNCs by a modified hot injection method. This conventional technique involves lead halide precursors being completely dissolved in octadecene (ODE), oleic acid (OA), and oleylamine (OLm) solution medium at 120 °C for 1 h under vacuum, subsequently rising temperature to 170 °C under Ar atmosphere. At this point, the PMA was introduced into the reaction mixture before injection of Cs-a precursor to avoid any potential disruption of PNCs after their formation. Later, the PNCs are subjected to centrifugation, separation, and subsequent redispersion of the perovskite nanocrystals into the toluene. The presence of a protective PMA polymer during the growth of the nanocrystals makes their processing easier by stopping them from aggregating. Later, the structure, PL mechanism, and environmental stability of these PNCs were analyzed. Furthermore, by incorporating PMA-encapsulated CsPbBr$_3$ PNCs into the phosphor layer of a white LED, we achieved a wide color gamut and improved luminescence efficiency, color rendering index (CRI), color temperature, and overall device performance.

2. Experimental materials and methods

Lead bromide (PbBr$_2$, 99.99 %, Sigma-Aldrich), cesium carbonate (Cs$_2$CO$_3$, 99.99 %, Sigma-Aldrich), 1-octadecene (ODE, 90 %, Sigma-Aldrich), oleic acid (OA, 90 %, Sigma-Aldrich), oleylamine (OLm, 80–90 %, Sigma-Aldrich), poly (maleic anhydride-alt-1-

octadecene) (PMA) (99.99 %, Sigma-Aldrich, molecular weight = 30,000−50,000), n-hexane (95.0 %, Samchun), and toluene (99.99 %, Samchun) were purchased and used without further purification.

2.1. Synthesis methodology

2.1.1. Cesium-oleate preparation

Cs_2CO_3 (0.204 g), 10 mL of ODE, and 0.6 mL of OA were loaded into a 50-mL three-neck flask, heated under vacuum to 120 °C for 1 h, and then heated under an Ar environment at 150 °C until Cs_2CO_3 was dissolved entirely, and a clear solution was obtained.

2.1.2. CsPbBr₃ PNCs synthesis

$CsPbBr_3$ PNCs were synthesized by loading ODE (5 mL) and 0.2 mmol of $PbBr_2$ into a 50 mL 3-neck flask and dried under vacuum at 120 °C for 1 h and then followed by heating the solution under Ar gas. Dried OA (0.5 mL) and OAm (0.5 mL) at 100 °C were injected at 150 °C under Ar gas. After complete solubilization of a $PbBr_2$ salt, the temperature was raised to 180 °C, and Cs-oleate solution (0.5 mL) was swiftly injected into the $PbBr_2$-ODE solution. After 60 s, the solution was immediately cooled to room temperature by immersing the flask in an ice-water bath. After the reaction, the crude NCs were separated by centrifugation and the residue was redispersed in 15 mL toluene, and the process was repeated. Later, the obtained PNCs were dispersed in the 5 mL toluene and transferred to the glovebox until further used.

2.1.3. CsPbBr₃/PMA PNC synthesis

A 50-mL three-neck flask is loaded with $PbBr_2$ (0.2 mmol) and ODE (5 mL) heated under vacuum at 120 °C for 1 h. The solution is then heated to 150 °C under an Ar gas. Dried OA and OAm (0.5 mL each) at 100 °C were injected into the $PbBr_2$-ODE solution at 150 °C under an Ar environment. After complete solubilization of the $PbBr_2$ salt, a clear solution was obtained. 215 mg of PMA was then added to the clear solution and allowed to react for 10 min. The temperature was then increased to 180 °C, and 0.5 mL of a Cs-oleate solution was quickly injected into the $PbBr_2$/PMA-ODE solution, which was promptly cooled to room temperature using ice-water bath after 60 s. After the reaction, the crude NCs were separated by centrifugation and the residue was redispersed in 15 mL toluene, and the process was repeated. Later, the obtained PNCs were dispersed in the 5 mL toluene and transferred to the glovebox until further used.

2.1.4. Design of a CsPbBr₃/PMA-coated LED device

For the construction of the prototype white-LED device, green-emitting $CsPbBr_3$/PMA PNCs were drop-casted onto a glass plate, and, similarly, K_2SiF_6:Mn^{4+} was mixed in a PMMA/toluene solution and drop-casted on a glass plate. The two plates were allowed to dry at room temperature to evaporate the toluene. The two glass plates were integrated into a 455-nm GaN blue LED.

2.2. Characterizations

The obtained PNCs were further characterized by XRD recorded using Bruker DE/D8 Advance X-ray Diffractometer, TEM
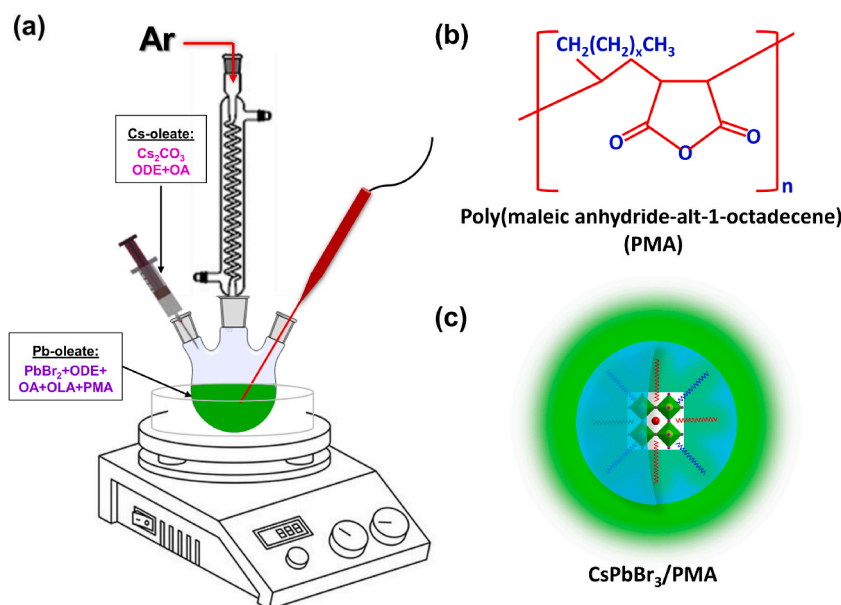

Fig. 1. (a) Schematic illustration of the synthesis procedure of CsPbBr₃/PMA PNCs using a modified one-pot hot-injection method, (b) structure of PMA, and (c) PMA polymer-coated CsPbBr₃ structure.

employing JEOL JEM-2100 electron microscope operated at 200 kV accelerating voltage, UV–vis absorption spectroscopy recorded using Shimadzu UV-2600 spectrometer, FT-IR spectroscopy recorded using Nicolet-5700 FT-IR spectrometer, PL spectroscopy employing Shimadzu RF-6000 Spectro-fluoro-photometer, TRPL recorded using HORIBA Jobin Yvon FluoroMax-4 fluorescence spectrometer. The PLQY of the PNCs dispersed toluene solutions were recorded using Shimadzu RF-6000 Spectro-fluoro-photometer using toluene as a reference under ambient conditions. The TA measurements used a Ti: sapphire regenerative amplifier system (LIBRA-USP-HE, Coherent, Inc.), which generated fundamental pulses centered at 805 nm (50 fs, 1 kHz rep. rate). Pump pulses of 100–200 nJ were produced at 480 and 403 nm, respectively, using a home-built noncollinear optical parametric amplifier and a sum-harmonic generation in a BBO crystal. The supercontinuum pulses in a sapphire window were measured using a fiber-based spectrometer with a back-illuminated CCD detector (QE65pro, Ocean Optics). Electroluminescence spectra were measured on a Labsphere CdS-610 spectrometer. The UV resistance measurement was carried out on freshly synthesized $CsPbBr_3$ and $CsPbBr_3$/PMA PNC solutions taken in vial by continuous irradiation using a UV lamp (365 nm, 6 W) kept at a distance of 10 cm for 75 days. To evaluate the moisture stability of uncoated and coated PNC solutions, 1.5 mL of each solution was immersed in 1.5 mL of deionized water for seven days. Temperature stability tests were conducted for the PNC powders under various temperatures.

3. Results and discussion

Fig. 1a illustrates the synthesis of $CsPbBr_3$/PMA PNCs by employing a modified hot-injection method, Fig. 1b displays the structure of PMA, and Fig. 1c shows the PMA polymer-coated $CsPbBr_3$ structure. The TEM images of the pristine $CsPbBr_3$ (Fig. 2a) and $CsPbBr_3$/PMA PNC (Fig. 2c) reveal that at a reaction time of 30 s (30 s after the injection of Cs-oleate) the NCs with cubic morphology are formed. Both PNC systems exhibited a well-defined pattern in the HRTEM images (Fig. 2b–d), suggesting a highly crystalline structure. The HRTEM images of pristine and coated PNCs show a lattice spacing of 0.58 nm, corresponding to the (100) planes, confirming the cubic crystal structure [8]. Additionally, the HRTEM images reveal that the lattice spacing remains consistent in both the pristine and coated PNCs, further confirming the preservation of the cubic crystal structure upon coating. These findings demonstrate the successful synthesis of highly crystalline $CsPbBr_3$/PMA PNCs with a well-defined morphology and uniform coating. The XRD patterns of the pristine and coated PNCs are presented in Fig. 2e. The diffraction patterns of the pristine and coated PNCs are well indexed with *Pm-3m* cubic $CsPbBr_3$ (JCPDS card no: 54–0752) [16]. The diffraction pattern observed in the pristine and coated PNCs indicates that both PNCs have the same crystal structure, further supporting the preservation of the $CsPbBr_3$ crystal structure upon coating and confirming the high crystallinity of the synthesized PNCs. The absence of any additional peaks suggests the absence of impurities, or the formation of a secondary phase suggests the formation of high-purity PNCs. The XRD results provide strong evidence for successfully synthesizing high crystalline $CsPbBr_3$/PMA PNCs with a uniform coating. The two materials displayed excellent uniformity and monodispersity, with a narrow size distribution at 9.51 and 9.90 nm, respectively (Fig. S1). The TEM and HRTEM images, along with the XRD patterns, reveal that both the pristine $CsPbBr_3$ and $CsPbBr_3$/PMA PNCs have a highly crystalline, cubic structure with excellent uniformity and monodispersity. These characteristics can contribute to the stability and enhanced optical properties of the NCs. Fig. S2 shows the Fourier transform infrared (FTIR) spectra measured for $CsPbBr_3$ and $CsPbBr_3$/PMA PNCs to understand the interaction between vibrational modes of PNCs and the PMA polymer matrix. On comparing the FTIR Spectra of $CsPbBr_3$ and $CsPbBr_3$/PMA PNCs, they almost exhibit identical characteristic vibrational bands, although with varying intensities. However, the main difference in the FTIR spectra of pristine and PMA-coated $CsPbBr_3$ PNCs lies with the presence of additional vibrational bands at around 1786 cm^{-1}, which is
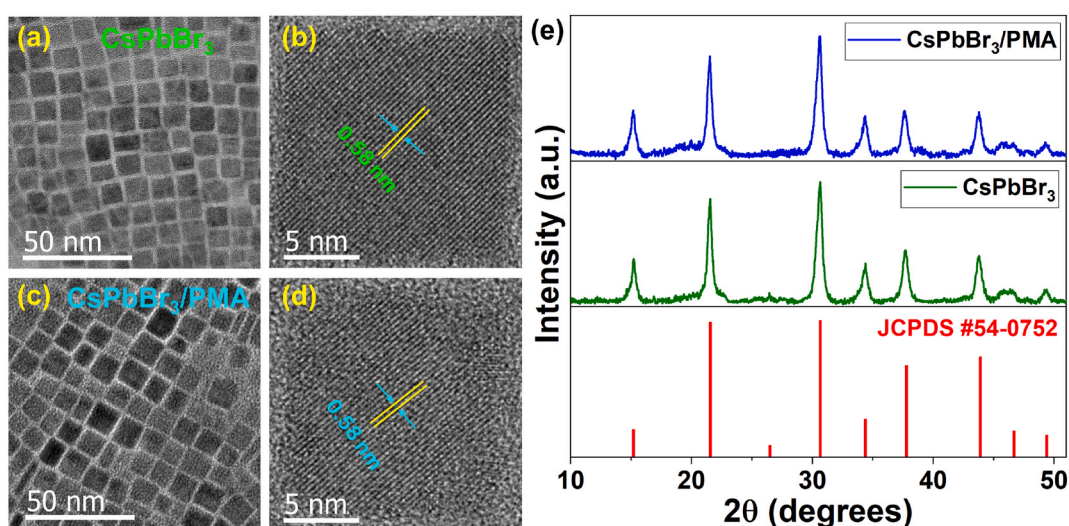

Fig. 2. (a, c) TEM and (b, d) HRTEM images of $CsPbBr_3$ and $CsPbBr_3$/PMA PNCs, respectively, and (e) XRD patterns of $CsPbBr_3$ (green trace) and $CsPbBr_3$/PMA PNCs (blue trace) and the standard XRD pattern for cubic $CsPbBr_3$ (PDF#54–0752). (For interpretation of the references to color in this figure legend, the reader is referred to the Web version of this article.)

attributed to the stretching vibrations of carbonyl (C=O) emanating from the anhydride group of the PMA polymer. The vibrational band at around 1267 cm^{-1} is associated with the stretching vibrations of the C–O group, which arises due to the anhydride group. Therefore, the emergence of C=O and C–O groups strongly indicates that the PNC surface is coated with PMA [8,31].

Fig. 3a and b demonstrate absorption and PL spectral profiles of the pristine and coated PNCs, respectively. The absorption spectra of the pristine and coated PNCs exhibit absorption onsets at 509 and 516 nm, respectively. The absorption edges of the pristine and coated PNCs are estimated to be 2.43 and 2.40 eV, respectively. Fig. 3c shows photographs of the pristine and coated PNCs in a colloidal solution under day and UV lights. The CsPbBr$_3$ PNCs exhibited a robust green emission at 516 nm, characterized by a small FWHM of 18.7 nm. On the other hand, the CsPbBr$_3$/PMA exhibited a strong green emission centered at around 522 nm, with an FWHM of 21.2 nm. The absorption and PL spectra of PMA-coated PNCs displayed a slight redshift compared to those of the pristine PNCs. This shift can be attributed to the quantum confinement effect, resulting from the increase in particle size due to the PMA coating of CsPbBr$_3$ PNCs. Additionally, multiple factors are involved in the redshift, such as defect transitions, thermal effects, and reabsorption effects caused by the overlap of the absorption band edge with the PL emission (spontaneous emission spectrum) contribute to the peak shift [19,33]. Furthermore, the coated PNCs appear to have a higher intensity of green emission than the pristine PNCs, suggesting that the coating has enhanced the photoluminescence efficiency of the CsPbBr$_3$ material. Considering these spectral features, we intended to measure the PLQY for the pristine and PMA-coated PNCs. The CsPbBr$_3$/PMA PNCs exhibit a PLQY of 86.8 %, greater than the PLQY of CsPbBr$_3$ (54.2 %) (Fig. S3) attributed to decrease in surface defects from effective passivation by PMA. When the PMA polymer was added to the precursor solution during the synthesis, the polymer was more tightly bound to the ligands on the surface of PNCs. Additionally, the PMA on the surface of the CsPbBr$_3$ PNCs decreases the number of surface dangling bonds, increasing the PL intensity. However, this does not always lead to a blue shift in luminescence [8,34,35].

The PL decay kinetics of the PNCs were investigated to comprehend the underlying mechanism responsible for the increase in the PLQY (Fig. 3d). By analyzing the emission intensity as a function of time, it is possible to extrapolate the PL lifetimes and decay components from the TRPL spectra. The PL decay spectra were subjected to a tri-exponential decay model (Eq. (1)). The average lifetimes were computed using Eq. (2) [36–38].

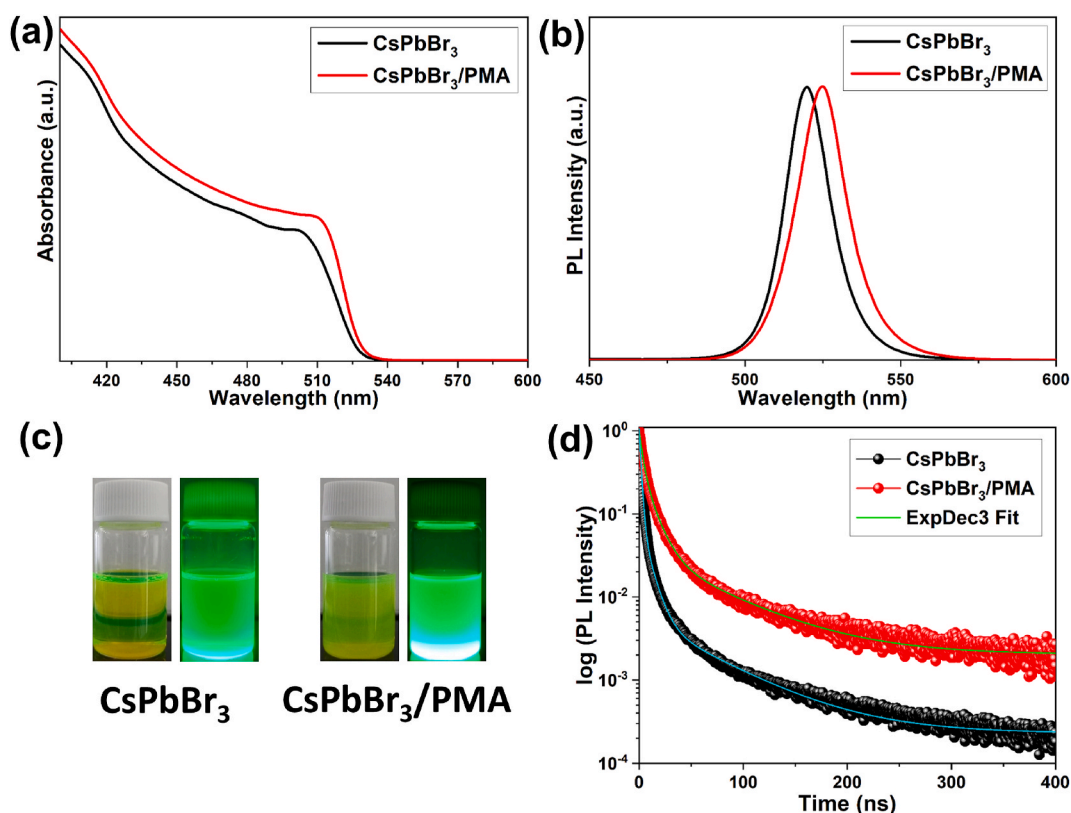$$C(t) = C_1 \exp\left(-t/\tau_1\right) + C_2 \exp\left(-t/\tau_2\right) + C_3 \exp\left(-t/\tau_3\right) \tag{1}$$

Fig. 3. (a) Absorption spectra of CsPbBr$_3$ (black trace) and CsPbBr$_3$/PMA (red trace) PNCs solutions. (b) PL spectra of CsPbBr$_3$ (black trace) and CsPbBr$_3$/PMA (red trace) PNCs solutions. (c) Photographs of the colloidal solutions of CsPbBr$_3$ and CsPbBr$_3$/PMA PNCs. (d) TRPL spectra of the CsPbBr$_3$ (black trace) and CsPbBr$_3$/PMA (red trace) PNCs solutions. (For interpretation of the references to color in this figure legend, the reader is referred to the Web version of this article.)

$$\tau_{av} = \left(C_1\tau_1^2 + C_2\tau_2^2 + C_3\tau_3^2 \right) \big/ \left(C_1\tau_1 + C_2\tau_2 + C_3\tau_3 \right) \tag{2}$$

where the lifetime component (τ_1) and its amplitude (C_1) are related to the intrinsic exciton relaxation, the intermediate lifetime component (τ_2) and its amplitude (C_2) corresponds to the phonon-exciton interactions, and the ultralong-lived lifetime component (τ_3) and its amplitude (C_3) are associated with the interactions between excitons and defects. The prolonged lifetime component (τ_3) may result from the reduced nonradiative energy transfer to trap states [36–39]. Fig. 3d reveals that the emission lifetime of the coated PNCs (23.5 ns) is longer than that of the pristine (12.8 ns). The extended decay time is attributed to surface passivation, i.e., suppression of surface defects on the pristine PNCs. Consequently, surface passivation increases the average lifetime and decreases the surface recombination velocity compared to the uncoated CsPbBr$_3$ PNCs. In addition, as a result of the delayed PL relaxation dynamics (extended decay time), which results from a reduction in the nonradiative recombination pathways and density of surface-trap defect states due to self-passivation, the PMA-coated PNCs have a significantly higher intensity than the uncoated PNCs. These findings are partially attributed to the suppression of surface defects on the uppermost surface of the PNCs. In addition to the TRPL decay analysis, we investigated the recombination dynamics of the CsPbBr$_3$ and CssPbBr$_3$/PMA PNCs and obtained the radiative (k_r) and nonradiative (k_{nr}) decay rates and radiative to nonradiative recombination ratio (k_r/k_{nr}) using the PLQYs and lifetimes (Table S1) [22]. The CsPbBr$_3$/PMA has a low nonradiative recombination rate ($k_{nr} = 0.0063$ ns^{-1}) and better radiative recombination rate ($k_r = 0.0402$ ns^{-1}) than that of the CsPbBr$_3$ PNCs, which indicates fewer traps owing to the suppression of nonradiative routes resulted from PMA coating. The k_r/k_{nr} ratio for the CsPbBr$_3$/PMA (6.35) is considerably better than that for CsPbBr$_3$ (0.842), which suggests that the PMA coating can reduce the nonradiative routes. According to the longer lifetime and higher k_r/k_{nr}, the CsPbBr$_3$/PMA contains fewer trap states compared to CsPbBr$_3$ as a result of the effective passivation of the CsPbBr$_3$ surface by PMA.

To better comprehend the impact of the surface passivation on the PNCs and to investigate the ultrafast exciton relaxation and recombination kinetics femtosecond transient absorption spectroscopy (fs-TAS) was performed. Fig. 4a–c shows TA spectra of CsPbBr$_3$ and CsPbBr$_3$/PMA measured in the region of 430–600 nm at an excitation at 400 nm at an energy of 4 nJ/pulse under various time intervals. Based on previous reports [40–42], TA spectra recorded in this spectral window show multiple features. First, strongly quantum-confined QDs have a positive photo-induced absorption band (PA1, $A > 0$) in the 441–496 nm region due to a forbidden exciton transition induced by the band-edge excitons. Second, the Stark effect, which results from the Coulombic interaction between
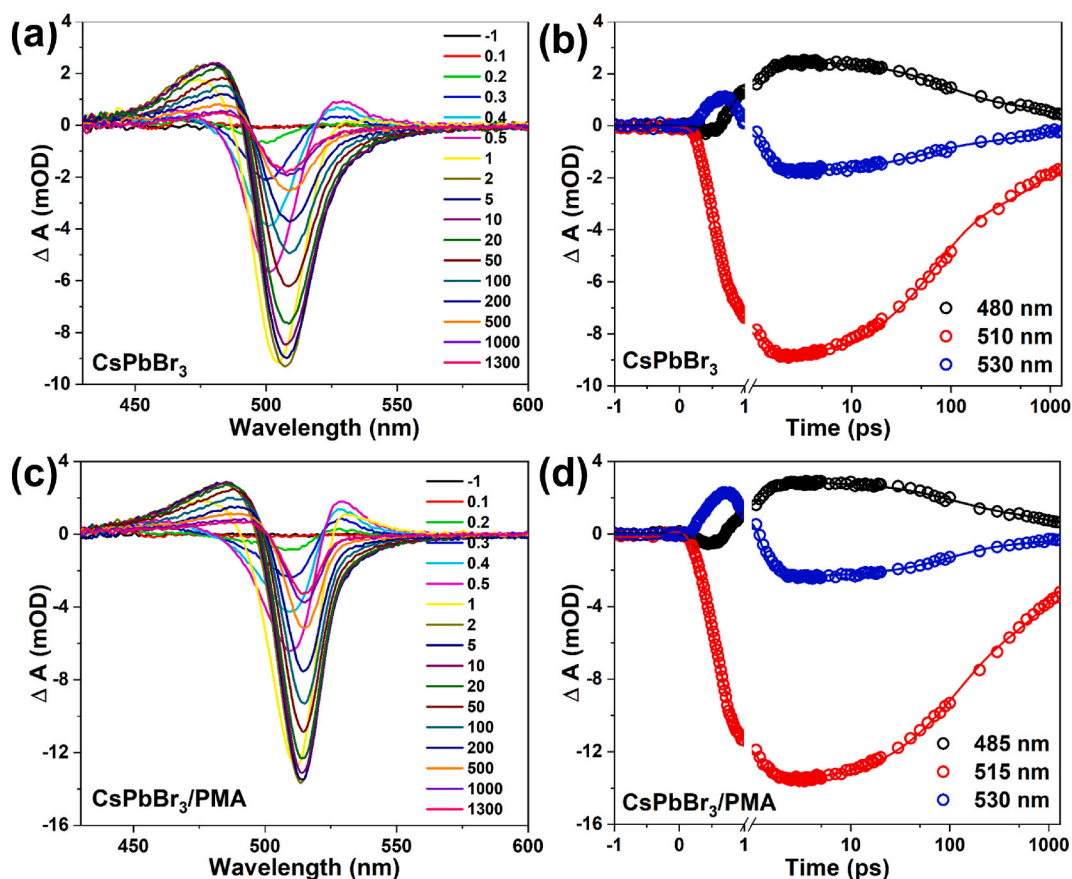

Fig. 4. Fs-TA absorption spectra of (a) CsPbBr$_3$ and (c) CsPbBr$_3$/PMA measured for different pump–probe delay times at excitation at 400 nm. Excited-state kinetic spectra for the bleach signal and positive absorption bands of (b) CsPbBr$_3$ and (d) CsPbBr$_3$/PMA.

band-edge excitons and hot carriers, is attributed to a short-lived absorption band (PA2) in the 521–560 nm wavelength region. Third, a ground-state bleach signal (GSB, $\Delta A < 0$) at 510 nm for $CsPbBr_3$ and 515 nm for the $CsPbBr_3$/PMA PNCs is identified from which charge carrier density on the bandgap can be determined [40–43]. The GSB signal is the first exciton absorption peak at the steady-state onset. Both samples exhibited narrow GSB signals due to charge carrier localization, indicating regularity in nanocrystal sizes. In both samples show that the negative GSB signals become progressively broader during the initial time delay, spanning a wide wavelength range, and reach high levels at approximately 2 ps because of state filling. With increase in delay time the signals become narrow and symmetric indicating a gradual recovery. This broadening of the GSB signals during the initial increase in time delay results from the time necessary to attain a quasi-thermal distribution of charge carrier density, which depends on the temperature variation between the carriers and lattice in the dark. Fig. 4b–d shows that the intensity of the GSB signals for $CsPbBr_3$/PMA is higher than that of $CsPbBr_3$. This suggests that PMA can suppress the defect surface states of $CsPbBr_3$ PNCs, eliminating trap fillings. The increased intensity of the bleach signal of $CsPbBr_3$/PMA compared to $CsPbBr_3$ is because of an increment in charge carrier density in the $CsPbBr_3$/PMA PNC core–shell-like system. The GSB trends in the TA profiles for $CsPbBr_3$ and $CsPbBr_3$/PMA are consistent with those reported for core–shell materials [31,43–45]. With the increase in the delay time, the bleach signals in the TA spectra of both perovskite systems undergo a longer wavelength shift, suggesting different relaxation pathways from the initial excited state resulting from laser pumping. As a result of exciton–exiton interactions, PA1 and PA2 exhibit a subtle longer wavelength shift in the initial picoseconds, and their intensity decreases as the delay time progresses. This phenomenon results from the rapid population of charge carriers at the band edges following intraband cooling, resulting in a state-filling-induced bleach, which predominates the spectral profiles and depletion of the Stark effect generated by carriers. After reaching their maximum intensities at 20 and 0.5 ps, the strengths of the absorption bands PA1 and PA2 gradually diminish. Fig. 4a–c shows TA kinetic curves of the bleach (GSB) and PA1 and PA2 bands at particular wavelengths for $CsPbBr_3$ and $CsPbBr_3$/PMA, spanning a time delay in the range of 0–1200 ps. Both samples show a rising component along with two decay components. A tri-exponential model is employed to provide the recovery dynamics of the GSB signals of the two samples. The time constants τ_1 (shorter), τ_2 (longer), and τ_3 (ultra longer) correspond to the hot-exciton intraband cooling, exciton trapping to bandgap trap states, and exciton recombination processes, respectively [31,41,42]. The time constants are determined to be $\tau_1 = 0.32$ ps, $\tau_2 = 63$ ps, and $\tau_3 = 1.22$ ns for $CsPbBr_3$, and $\tau_1 = 0.26$ ps, $\tau_2 = 86$ ps, and $\tau_3 = 1.46$ ns for $CsPbBr_3$/PMA. Due to the reduced surface trap states, longer excitation lifetimes of $CsPbBr_3$/PMA are observed, indicating an effective passivation of the $CsPbBr_3$ surface by PMA.

A UV resistance test (Fig. 5a) was performed by continuously irradiating the $CsPbBr_3$ and $CsPbBr_3$/PMA PNCs under UV light. After
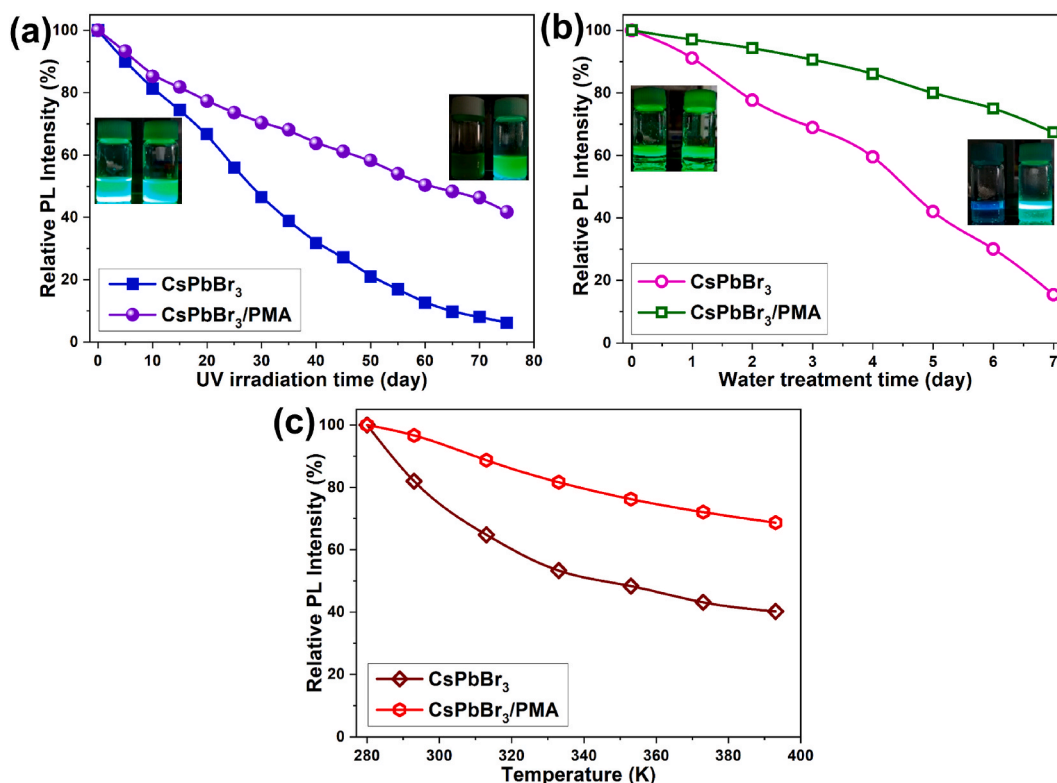

Fig. 5. (a) Relative PL intensity of pristine $CsPbBr_3$ (blue trace) and $CsPbBr_3$/PMA (violet trace) solutions against UV light (photostability test). (b) Relative PL intensity of pristine $CsPbBr_3$ (magenta trace) and $CsPbBr_3$/PMA (green trace) solutions against storage time in water (water stability test). (c) Relative PL intensity of pristine $CsPbBr_3$ (red trace) and $CsPbBr_3$/PMA (wine red trace) solutions at different temperatures (thermal stability test). (For interpretation of the references to color in this figure legend, the reader is referred to the Web version of this article.)

75 days of continuous UV irradiation, the $CsPbBr_3$ PNCs retained only 6.2 % of their initial emission intensity, while the $CsPbBr_3$/PMA PNCs retained 42.4 %, demonstrating good UV resistance. This decrease in emission intensity can be attributed to the degradation of $CsPbBr_3$ PNCs under UV light, leading to the detachment of surface ligands. Consequently, defects and clusters on the surface of CsPbBr3 PNCs occur, significantly reducing their emission intensity. Conversely, the $CsPbBr_3$/PMA PNCs exhibit better UV resistance, as the presence of PMA as a surface ligand prevents the desorption and degradation of $CsPbBr_3$ PNCs, thereby maintaining a higher emission intensity even after prolonged UV irradiation. This enhanced UV resistance of $CsPbBr_3$/PMA PNCs suggests that PMA effectively stabilizes the surface of $CsPbBr_3$ PNCs. Water resistance experiments were conducted by adding 1.5 mL of each colloidal solution of $CsPbBr_3$ and $CsPbBr_3$/PMA PNCs into vials containing 1.5 mL water under ambient conditions for seven days (Fig. 5b). Following the seven days of exposure, the emission intensities of the two PNC materials decreased, with the $CsPbBr_3$ PNCs having a more significant decrease than the $CsPbBr_3$/PMA PNCs. The PL intensity of the pure CsPbBr3 PNCs decreased to 14.1 % because of the aggregation of the ligand-protected $CsPbBr_3$ PNCs upon exposure to moisture. This aggregation phenomenon was attributed to the weak bonding between ligands and the $CsPbBr_3$ surface, which made the $CsPbBr_3$ PNCs susceptible to moisture-induced degradation. On the other hand, the $CsPbBr_3$/PMA PNCs demonstrated a higher PL retention capability of 68.9 % due to the protective barrier provided by the PMA matrix, which prevented moisture from reaching the PNC surface and causing aggregation. In addition, a thermal resistance test (Fig. 5c) for $CsPbBr_3$ and $CsPbBr_3$/PMA PNCs was carried out in the temperature range of 280–393 K. The thermal stability of the $CsPbBr_3$/PMA PNCs was 71.3 % higher than that of the $CsPbBr_3$ PNCs, which had a thermal resistance of 39.5 %. The PL emission intensities of both PNCs decrease with the increase in temperature due to increase in electron–phonon interaction with increase in temperature, leading to enhanced nonradiative recombination and reduced PL intensity. The presence of capping ligands on the surface of the PNCs can form surface energy states within the forbidden gap of the PNCs, resulting in a reduction of the PL intensity [6,46–48]. These results indicate that $CsPbBr_3$/PMA PNCs exhibited excellent stability under UV irradiation, moisture and thermal treatments, highlighting their exceptional suitability for various potential applications, such as in LEDs. Because of the effective passivation by PMA, the $CsPbBr_3$/PMA PNCs exhibit superior stability over $CsPbBr_3$ PNCs.

Considering the high PLQY, exceptional optical performance, and environmental stability of $CsPbBr_3$/PMA, it can be used as a green-light-emitting component to fabricate a white LED. To fabricate a white LED, the green-emitting $CsPbBr_3$/PMA and red-emitting K_2SiF_6:Mn^{4+} were separately coated onto glass slides and integrated onto a commercial blue-LED chip ($\lambda_{emi} = 455$ nm) operating at 20 mA. Fig. 6a shows the EL spectra of the resultant white LEDs constructed using $CsPbBr_3$/PMA PNCs as green component. The inset in
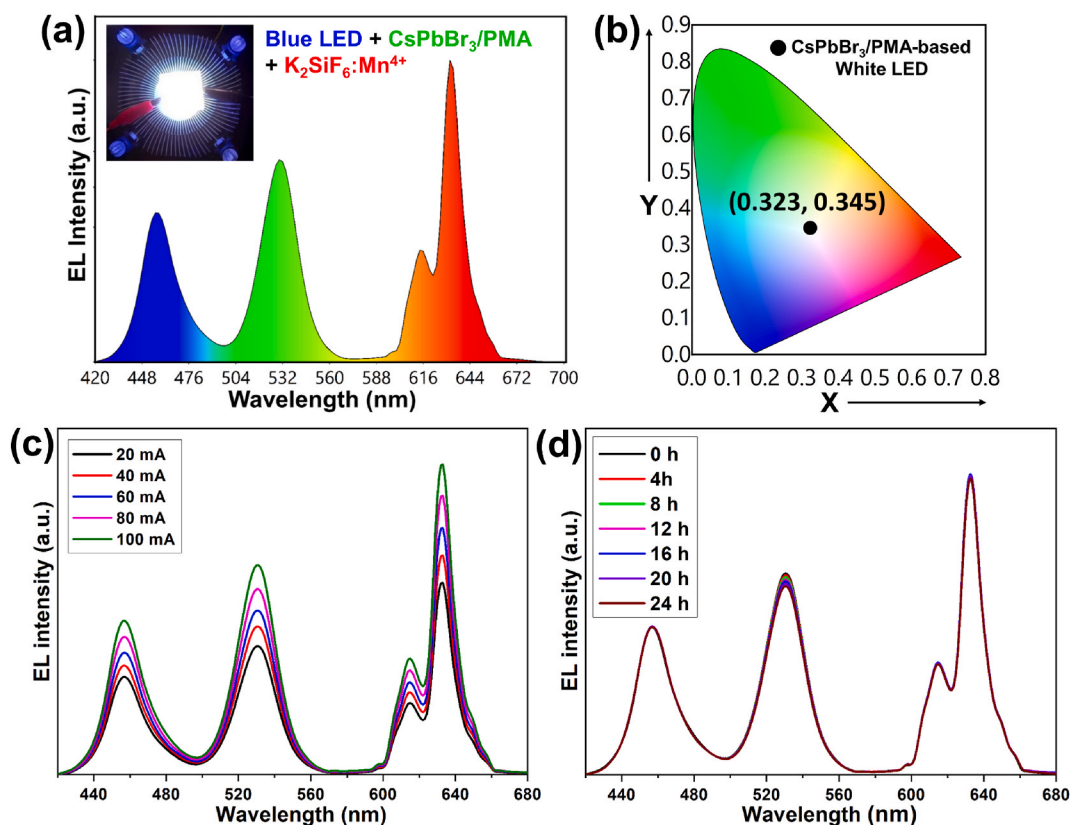

Fig. 6. (a) EL spectra of the white-LED device obtained by integrating $CsPbBr_3$/PMA and K_2SiF_6:Mn^{4+}-coated glass slides onto a 455-nm GaN LED (the inset image shows a photograph of the fabricated white-LED device) and (b) ICI diagram with white light coordinates of the white-LED device shown in (a). EL spectra of a constructed white LED device operated at (c) different operating currents and (d) different time intervals.

Fig. 6a is the photograph of the fabricated CsPbBr$_3$/PMA-based white-LED device generating white light under an operating current of 20 mA. The EL spectrum exhibited three distinctive peaks in red, green, and blue (RGB) regions at 455, 524, and 630 nm, respectively. Under a driving current of 20 mA, the white-LED device exhibits a luminous efficiency of 58.4 lm/W and CRI of 83.2 with a correlated color temperature of 5916 K and International Commission on Illumination (ICI) coordinates of (0.323, 0.345) (Fig. 6b). The white LED has an exceptionally wide color gamut, spanning 125.3 % of the National Television Standards Committee (NTSC) and 98.9 % of the Rec. 2020. For a comprehensive comparison, EL spectrum of the white LED constructed using pristine CsPbBr$_3$ was measured (Fig. S4a) and respective color coordinates are displayed in chromaticity diagram (Fig. S4b). Additionally, the EL parameters (LE, CRI, CCT and color coordinates) of the constructed pristine CsPbBr$_3$ and CsPbBr$_3$/PMA-based white LEDs are summarized in Table S2.

Stability is a key factor for the commercial viability of white LEDs, as it ensures consistent and reliable performance over a wide range of applied currents and durations. We further examined the performance of the constructed white-LED device under varying drive currents, within the 20–100 mA range (Fig. 6c). The electroluminescence (EL) spectra displayed distinct peaks corresponding to the of RGB emissions of blue-LED, CsPbBr$_3$/PMA, and K$_2$SiF$_6$:Mn^{4+} materials. As the forward-bias current increased from 20 mA to 100 mA, we observed an enhancement in emission intensities and a shift in their respective color coordinates from (0.323, 0.345) to (0.311, 0.327). This shift was accompanied by increased color temperature (CCT) from 5916 K to 6618 K, while CRI slightly declined from 83.2 to 74.7. However, the luminescence efficiency experienced a significant drop from 58.4 lm/W at 20 mA to 17.6 lm/W at 100 mA. This reduction in luminescence efficiency is likely due to the increase in non-radiative recombination processes at higher current levels. Furthermore, the EL spectra were captured at various time intervals to test the stability of white LED operating at 20 mA [49, 50]. The results showed that there is no significant variation in EL spectra even after 24 h of continues operation (Fig. 6d), suggesting that the white LED we constructed exhibits excellent stability, making it suitable for commercial use. The absence of spectral variation or shift implies that the LED can maintain its desired color temperature and color rendering properties, making it versatile for various lighting applications. The EL parameter (LE, CRI, and CCT) of our designed CsPbBr$_3$/PMA-based white-LED device is shown in Fig. S5. Finally, we compared the PLQY, stability, LE, CRI and color gamut (NTSC%) of currently synthesized CsPbBr$_3$/PMA with the other polymer like PMMA-coated CsPbBr$_3$ and summarized in Table S3.

4. Conclusion

CsPbBr$_3$ and CsPbBr$_3$ coated PMA (CsPbBr$_3$/PMA) PNCs have been successfully synthesized using a modified hot-injection method. The absorption and PL spectra of PMA-coated PNCs displayed a slight redshift compared to those of the pristine PNCs, which can be attributed to the quantum confinement effect resulting from the increase in particle size due to the PMA coating of CsPbBr$_3$ PNCs. The CsPbBr$_3$/PMA PNCs exhibited an improved PLQY of 86.8 % compared to that of CsPbBr$_3$ PNCs of 54.2 % due to the passivation of surface defects reducing non-radiative recombination pathways, resulting in improved PLQY. The TRPL spectra and transient absorption measurements revealed longer lifetimes for CsPbBr$_3$/PMA PNCs because of the effective passivation of surface defects by PMA coating. Additionally, the CsPbBr$_3$/PMA PNCs exhibited good stability against UV light, moisture, and temperature, retaining 42.4 %, 68.9 %, and 71.3 % of initial PL intensity, respectively. The enhancement can be attributed to the polymer coating, which uses its ligands to connect with the uncoordinated Pb and Br ions on the surface of PNCs and avoid exposure to the external environment. Furthermore, to demonstrate the potential application of CsPbBr$_3$/PMA in down-conversion white LEDs, we integrated the green-emitting CsPbBr$_3$/PMA and red K$_2$SiF$_6$:Mn^{4+} phosphor-coated glass slides to a 455-nm blue-LED. The resulting white LED emitted a bright white light with ICI color coordinates of (0.323, 0.345), luminous efficiency of 58.4 %, and CRI of 83.2. The fabricated white-LED system also attained a wide color gamut of 125.3 % of NTSC and 98.9 % of Rec. 2020. These findings highlight the potential of CsPbBr$_3$/PMA as an efficient down-conversion material for white LEDs and backlighting applications.

Author contributions

Si-Hyun Park: Writing – review & editing, Supervision, Resources, Project administration, Funding acquisition. M. Chandra Sekhar: Resources. Youngsuk Suh: Resources. C. Kamal Basha: Methodology, Investigation, Formal analysis. S. Sreedhar: Methodology, Investigation, Formal analysis. B. Jagadeesh Babu: Methodology, Investigation, Formal analysis. Bommireddy Purusottam Reddy: Writing – original draft, Software, Funding acquisition, Formal analysis, Data curation, Conceptualization

Data availability statement

Data will be made available on request.

Declaration of competing interest

The authors declare that they have no known competing financial interests or personal relationships that could have appeared to influence the work reported in this paper.

Acknowledgments

Appendix A. Supplementary data

Supplementary data to this article can be found online at https://doi.org/10.1016/j.heliyon.2024.e24497.

Abbreviations

perovskite nanocrystal   (PNC)
poly(maleic anhydride-alt-1-octadecene)   (PMA)
light-emitting diode   (LED)
photoluminescence quantum yield   (PLQY)
quantum dot   (QD)
color rendering index   (CRI)
1-octadecene   (ODE)
oleic acid   (OA)
X-ray diffraction   (XRD)
transmission electron microscopy   (TEM)
ultraviolet–visible   (UV–vis)
photoluminescence   (PL)
time-resolved PL   (TRPL)
transient absorption   (TA)
electroluminescence   (EL)
full width at half maximum   (FWHM)
femtosecond transient absorption spectroscopy   (fs-TAS)
ground-state bleach   (GSB)

References

[1] L. Protesescu, S. Yakunin, M.I. Bodnarchuk, F. Krieg, R. Caputo, C.H. Hendon, R.X. Yang, A. Walsh, M.V. Kovalenko, Nanocrystals of cesium lead halide perovskites ($CsPbX_3$, X = Cl, Br, and I): novel optoelectronic materials showing bright emission with wide color gamut, Nano Lett. 15 (2015) 3692–3696.
[2] S.D. Stranks, G.E. Eperon, G. Grancini, C. Menelaou, M.J.P. Alcocer, T. Leijtens, L.M. Herz, A. Petrozza, H.J. Snaith, Electron-hole diffusion lengths exceeding 1 micrometer in an organometal trihalide perovskite absorber, Science 342 (2013) 341–344.
[3] J. Qin, X.-K. Liu, C. Yin, F. Gao, Carrier dynamics and evaluation of lasing actions in halide perovskites, Trends Chem 3 (2021) 34–46.
[4] J. Shamsi, A.S. Urban, M. Imran, L. De Trizio, L. Manna, Metal halide perovskite nanocrystals: synthesis, post-synthesis modifications, and their optical properties, Chem. Rev. 119 (2019) 3296–3348.
[5] C.-Y. Huang, H. Li, Y. Wu, C.-H. Lin, X. Guan, L. Hu, J. Kim, X. Zhu, H. Zeng, T. Wu, Inorganic halide perovskite quantum dots: a versatile nanomaterial platform for eelectronic applications, Nano-Micro Lett. 15 (2022) 16.
[6] V. Naresh, B.H. Kim, N. Lee, Synthesis of $CsPbX_3$ (X = Cl/Br, Br, and Br/I)@SiO_2/PMMA composite films as color-conversion materials for achieving tunable multi-color and white light emission, Nano Res. 14 (2021) 1187–1194.
[7] M. Palei, M. Imran, G. Biffi, L. Manna, F. Di Stasio, R. Krahne, Robustness to high temperatures of Al_2O_3- coated $CsPbBr_3$ nanocrystal thin films with high-photoluminescence quantum yield for light emission, ACS Appl. Nano Mater. 3 (2020) 8167–8175.
[8] M. Meyns, M. Perálvarez, A. Heuer-Jungemann, W. Hertog, M. Ibáñez, R. Nafria, A. Genç, J. Arbiol, M.V. Kovalenko, J. Carreras, A. Cabot, A.G. Kanaras, Polymer-enhanced stability of inorganic perovskite nanocrystals and their application in color conversion LEDs, ACS Appl. Mater. Interfaces 8 (2016) 19579–19586.
[9] Y.H. Nam, K. Han, W.J. Chung, W.B. Im, Double Encapsulation of $CsPbBr_3$ perovskite nanocrystals with inorganic glasses for robust color converters with wide color gamut, ACS Appl. Nano Mater. 4 (2021) 7072–7078.
[10] V. Naresh, N. Lee, Zn(II)-doped cesium lead halide perovskite nanocrystals with high quantum yield and wide color tunability for color-conversion light-emitting displays, ACS Appl. Nano Mater. 3 (2020) 7621–7632.
[11] C. Zhang, J. Chen, L. Kong, L. Wang, S. Wang, W. Chen, R. Mao, L. Turyanska, G. Jia, X. Yang, Core/shell metal halide perovskite nanocrystals for optoelectronic applications, Adv. Funct. Mater. 31 (2021) 2100438.
[12] G.H. Ahmed, J. Yin, O.M. Bakr, O.F. Mohammed, Successes and challenges of core/shell lead halide perovskite nanocrystals, ACS Energy Lett. 6 (2021) 1340–1357.
[13] S.-C. Hsu, Y.-M. Huang, C.-P. Huang, T.-Y. Lee, Y.-Y. Cho, Y.-H. Liu, A. Manikandan, Y.-L. Chueh, T.-M. Chen, H.-C. Kuo, C.-C. Lin, Improved long-term reliability of a silica-encapsulated perovskite quantum- dot light-emitting device with an optically pumped remote film package, ACS Omega 6 (2021) 2836–2845.
[14] S. Li, L. Nie, S. Ma, G. Yao, F. Zeng, X. Wang, C. Sun, G. Hu, Z. Su, Environmentally friendly $CsPbBr_3$ QDs multicomponent glass with super-stability for optoelectronic devices and up-converted lasing, J. Eur. Ceram. Soc. 40 (2020) 3270–3278.
[15] X. Wang, X. Lian, Z. Zhang, H. Gao, Could nanocomposites continue the success of halide perovskites? ACS Energy Lett. 4 (2019) 1446–1454.
[16] E. Fanizza, R. Schingo, A. Panniello, A.M. Lanza, N. Depalo, A. Agostiano, M.L. Curri, M. Striccoli, $CsPbBr_3$ nanocrystals-based polymer nanocomposite films: effect of polymer on spectroscopic properties and moisture tolerance, Energies 13 (2020) 6730.
[17] L.-C. Chen, C.-H. Tien, Z.-L. Tseng, Y.-S. Dong, S. Yang, Influence of PMMA on all-inorganic halide perovskite $CsPbBr_3$ quantum dots combined with polymer matrix, Materials 12 (2019) 985.
[18] S.M. Lee, H. Jung, W.I. Park, Y. Lee, E. Koo, J. Bang, Preparation of water-soluble $CsPbBr_3$ perovskite quantum dot nanocomposites via encapsulation into amphiphilic copolymers, Chem. Select. 3 (2018) 11320–11325.
[19] S.M.H. Qaid, H.M. Ghaithan, K.K. AlHarbi, B.A. Al-Asbahi, A.S. Aldwayyan, Enhancement of light amplification of $CsPbBr_3$ perovskite quantum dot films via surface encapsulation by PMMA polymer, Polymers 13 (2021) 2574.

[20] S.N. Raja, Y. Bekenstein, M.A. Koc, S. Fischer, D. Zhang, L. Lin, R.O. Ritchie, P. Yang, A.P. Alivisatos, Encapsulation of perovskite nanocrystals into macroscale polymer matrices: enhanced stability and polarization, ACS Appl. Mater. Interfaces 8 (2016) 35523–35533.

[21] Z. Wang, Z. Wei, Y. Cai, L. Wang, M. Li, P. Liu, R. Xie, L. Wang, G. Wei, H.Y. Fu, Encapsulation-enabled perovskite–PMMA films combining a micro-LED for high-speed white-light communication, ACS Appl. Mater. Interfaces 13 (2021) 54143–54151.

[22] J. Tong, J. Wu, W. Shen, Y. Zhang, Y. Liu, T. Zhang, S. Nie, Z. Deng, Direct Hot-injection synthesis of lead halide perovskite nanocubes in acrylic monomers for ultrastable and bright nanocrystal–polymer composite films, ACS Appl. Mater. Interfaces 11 (2019) 9317–9325.

[23] Y. Zhang, Y. Pan, J. Ni, Z. i Yan, N. Deng, W. Sun, W. Kang, In situ growth of $CsPbBr_3$@PS flexible fiber papers by one step electrospinning with high stability toward fluorescent sensor, J. Lumin. 259 (2023) 119832.

[24] K.J. Babu, G. Kaur, A. Shukla, A. Kaur, H. Bhatt, N. Ghorai, G. De, H.N. Ghosh, In situ $CsPbBr_3$ architecture engineered in electrospun fibers and its ultrafast charge-transfer dynamics, Mater. Adv. 3 (2022) 6566.

[25] M. Peng, S. Sun, B. Xu, Z. Deng, Polymer-encapsulated halide perovskite color converters to overcome blue overshoot and cyan gap of white light-emitting diodes, Adv. Funct. Mater. 33 (2023) 2300583.

[26] G.C. Adhikari, S. Thapa, H. Zhu, P. Zhu, UV resin enhanced stability of metal halide perovskite nanocrystals for white light-emitting diodes, ACS Appl. Electron. Mater. 2 (2020) 35–40.

[27] P. Zhu, S. Thapa, H. Zhu, D. Venugopal, A. Sambou, Y. Yue, S.S. Dantuluri, S. Gangopadhyay, Solid- state white light-emitting diodes based on 3D-printed $CsPbX_3$-resin color conversion layers, ACS Appl. Electron. Mater. (2023), https://doi.org/10.1021/acsaelm.2c01778.

[28] Y. Ling, Y. Tian, X. Wang, J.C. Wang, J.M. Knox, F. Perez-Orive, Y. Du, L. Tan, K. Hanson, B. Ma, H. Gao, Enhanced optical and electrical properties of polymer-assisted all-inorganic perovskites for light-emitting diodes, Adv. Mater. 28 (2016) 8983–8989.

[29] N.C. Bigall, A. Curcio, M.P. Leal, A. Falqui, D. Palumberi, R. Di Corato, E. Albanesi, R. Cingolani, T. Pellegrino, Magnetic nanocarriers with tunable pH dependence for controlled loading and release of cationic and anionic payloads, Adv. Mater. 23 (2011) 5645–5650.

[30] H. Li, H. Lin, D. Ouyang, C. Yao, C. Li, J. Sun, Y. Song, Y. Wang, Y. Yan, Y. Wang, Q. Dong, W.C.H. Choy, Efficient and stable red perovskite light-emitting diodes with operational stability >300 h, Adv. Mater. 33 (2021) 2008820.

[31] J. Xu, L. Zhu, J. Chen, S. Riaz, L. Sun, Y. Wang, W. Wang, J. Dai, Transient optical properties of $CsPbX_3$/poly(maleic anhydride-alt-1-octadecene) perovskite quantum dots for white light-emitting diodes, Phys. Status Solidi RRL (2020) 2000498.

[32] H. Wu, S. Wang, F. Cao, J. Zhou, Q. Wu, H. Wang, X. Li, L. Yin, X. Yang, Ultrastable inorganic perovskite nanocrystals coated with a thick long-chain polymer for efficient white light-emitting diodes, Chem. Mater. 31 (2019) 1936–1940.

[33] S.M.H. Qaid, H.M. Ghaithan, B.A. Al-Asbahi, A.S. Aldwayyan, Ultra-stable polycrystalline $CsPbBr_3$ perovskite–polymer composite thin disk for light-emitting applications, Nanomaterials 10 (2020) 2382.

[34] T. Liang, W. Liu, X. Liu, Y. Li, W. Wu, J. Fan, In situ phase-transition crystallization of all-inorganic water-resistant exciton-radiative heteroepitaxial $CsPbBr_3$–$CsPb_2Br_5$ core–shell perovskite nanocrystals, Chem. Mater. 33 (2021) 4948–4959.

[35] P. Reiss, M. Protière, L. Li, Core/shell semiconductor nanocrystals, Small 5 (2009) 154–168.

[36] Z. Hu, Z. Liu, Y. Bian, S. Li, X. Tang, J. Du, Z. Zang, M. Zhou, W. Hu, Y. Tian, Y. Leng, Enhanced two- photon-pumped emission from in situ synthesized nonblinking $CsPbBr_3$/SiO_2 nanocrystals with excellent stability, Adv. Opt. Mater. 6 (2018) 1700997.

[37] S. Sun, D. Yuan, Y. Xu, A. Wang, Z. Deng, Ligand-mediated synthesis of shape-controlled cesium lead halide perovskite nanocrystals via reprecipitation process at room temperature, ACS Nano 10 (2016) 3648–3657.

[38] Z. Liang, S. Zhao, Z. Xu, B. Qiao, P. Song, D. Gao, X. Xu, Shape-controlled synthesis of all-inorganic $CsPbBr_3$ perovskite nanocrystals with bright blue emission, ACS Appl. Mater. Interfaces 8 (2016) 28824–28830.

[39] V. Kumar, V. Nagal, R. Kumar, S. Srivastava, B.K. Gupta, M. Kumar, A.K. Hafiz, K. Singh, Influence of the rate of radiation energy on the charge-carrier kinetics application of all-inorganic $CsPbBr_3$ perovskite nanocrystals, RSC Adv. 10 (2020) 34651–34657.

[40] N. Mondal, A. De, S. Das, S. Paul, A. Samanta, Ultrafast carrier dynamics of metal halide perovskite nanocrystals and perovskite-composites, Nanoscale 11 (2019) 9796–9818.

[41] N. Mondal, A. Samanta, Complete ultrafast charge carrier dynamics in photo-excited all-inorganic perovskite nanocrystals ($CsPbX_3$), Nanoscale 9 (2017) 1878–1885.

[42] R. Wu, Q. Wang, S. Yang, L. Wu, S. Gong, Q. Han, W. Wu, Enhanced thermal stability of exciton recombination in $CsPbI_3$ perovskite nanocrystals via zinc alloying, J. Alloys Compd. 857 (2021) 157574.

[43] G. Kaur, K. Justice Babu, N. Ghorai, T. Goswami, S. Maiti, H.N. Ghosh, Polaron-mediated slow carrier cooling in a Type-1 3D/0D $CsPbBr_3$@Cs_4PbBr_6 core–shell perovskite system, J. Phys. Chem. Lett. 10 (2019) 5302–5311.

[44] Y. Wu, C. Wei, X. Li, Y. Li, S. Qiu, W. Shen, B. Cai, Z. Sun, D. Yang, Z. Deng, H. Zeng, In situ passivation of $PbBr_6^{4-}$ octahedra toward blue luminescent $CsPbBr_3$ nanoplatelets with near 100% absolute quantum yield, ACS Energy Lett. 3 (2018) 2030–2037.

[45] J.-F. Liao, Y.-F. Xu, X.-D. Wang, H.-Y. Chen, D.-B. Kuang, $CsPbBr_3$ nanocrystal/MO_2 (M = Si, Ti, Sn) composites: insight into charge-carrier dynamics and photoelectrochemical applications, ACS Appl. Mater. Interfaces 10 (2018) 42301–42309.

[46] J. Zhu, Z. Xie, X. Sun, S. Zhang, G. Pan, Y. Zhu, B. Dong, X. Bai, H. Zhang, H. Song, Highly efficient and stable inorganic perovskite quantum dots by embedding into a polymer matrix, Chem. Nano Mat. 5 (2019) 346.

[47] Z. Wang, R. Fu, F. Li, H. Xie, P. He, Q. Sha, Z. Tang, N. Wang, H. Zhong, One-step polymeric melt encapsulation method to prepare $CsPbBr_3$ perovskite quantum dots/polymethyl methacrylate composite with high performance, Adv. Funct. Mater. 31 (2021) 2010009.

[48] X. Zeng, L. Yu, K. Peng, Y. Yu, D. Sun, C. Miao, Y. Fu, Ultrastable FB@$CsPbBr_3$/PMMA composites based on in-situ passivation and encapsulation for WLED applications, J. Lumin. 261 (2023) 119910.

[49] F. Gao, W. Yang, X. Liu, Y. Li, W. Liu, H. Xu, Y. Liu, Highly stable and luminescent silica-coated perovskite quantum dots at nanoscale-particle level via nonpolar solvent synthesis, Chem. Eng. J. 407 (2021) 128001.

[50] X. Di, L. Shen, J. Jiang, M. He, Y. Cheng, L. Zhou, X. Liang, W. Xiang, Efficient white LEDs with bright green-emitting $CsPbBr_3$ perovskite nanocrystal in mesoporous silica nanoparticle, J. Alloys Compd. 729 (2017) 526–532.